HAL
open science

Insights into Solid-To-Solid Transformation of MOF Amorphous Phases

Yuri Mezenov, Stephanie Bruyere, Andrei Krasilin, Ekaterina Khrapova, Semyon Bachinin, Pavel Alekseevskiy, Sergei Shipiloskikh, Pascal Boulet, Sebastien Hupont, Alexandre Nominé,, et al.

To cite this version:

Yuri Mezenov, Stephanie Bruyere, Andrei Krasilin, Ekaterina Khrapova, Semyon Bachinin, et al.. Insights into Solid-To-Solid Transformation of MOF Amorphous Phases. Inorganic Chemistry, 2022, 61 (35), pp.13992-14003. 10.1021/acs.inorgchem.2c01978 . hal-03797175

HAL Id: hal-03797175

https://hal.science/hal-03797175v1

Submitted on 4 Oct 2022

HAL is a multi-disciplinary open access archive for the deposit and dissemination of scientific research documents, whether they are published or not. The documents may come from teaching and research institutions in France or abroad, or from public or private research centers.

L'archive ouverte pluridisciplinaire **HAL**, est destinée au dépôt et à la diffusion de documents scientifiques de niveau recherche, publiés ou non, émanant des établissements d'enseignement et de recherche français ou étrangers, des laboratoires publics ou privés.

Insights into Solid-To-Solid Transformation of MOF Amorphous Phases

Yuri A. Mezenov,[#] Stephanie Bruyere,[#] Andrei Krasilin, Ekaterina Khrapova, Semyon V. Bachinin, Pavel V. Alekseevskiy, Sergei Shipiloskikh, Pascal Boulet, Sebastien Hupont, Alexandre Nomine, Brigitte Vigolo, Alexander S. Novikov, Thierry Belmonte, and Valentin A. Milichko*

ABSTRACT: Metal–organic frameworks (MOFs) have been recently explored as crystalline solids for conversion into amorphous phases demonstrating non-specific mechanical, catalytic, and optical properties. The real-time control of such structural transformations and their outcomes still remain a challenge. Here, we use *in situ* high-resolution transmission electron microscopy with 0.01 s time resolution to explore non-thermal (electron induced) amorphization of a MOF single crystal, followed by transformation into an amorphous nanomaterial. By comparing a series of *M*-BTC (*M*: Fe^{3+}, Co^{3+}, Co^{2+}, Ni^{2+}, and Cu^{2+}; BTC: 1,3,5-benzentricarboxylic acid), we demonstrate that the topology of a metal cluster of the parent MOFs determines the rate of formation and the chemistry of the resulting phases containing an intact ligand and metal or metal oxide nanoparticles. Confocal Raman and photoluminescence spectroscopies further confirm the integrity of the BTC ligand and coordination bond breaking, while high-resolution imaging with chemical and structural analysis over time allows for tracking the dynamics of solid-to-solid transformations. The revealed relationship between the initial and resulting structures and the stability of the obtained phase and its photoluminescence over time contribute to the design of new amorphous MOF-based optical nanomaterials.

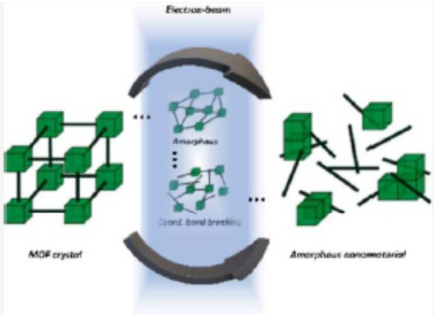

Crystalline metal–organic frameworks (MOFs) appeared to be promising solids for application as gas sorbents,[1] separators,[2] and new active elements in opto- and micro-electronic devices.[3−5] The highly ordered porous structure of MOFs provides an efficient and lossless propagation of mechanical,[6] thermal,[7] and electromagnetic energy,[8] as well as molecules[9] and charged particles along the structure,[10] which underlies the operation of the above devices. Meanwhile, the transformation of the parent crystal structure into various amorphous and liquid phases[11−15] allows for designing new MOF-based materials for which a long-range order plays a minor role. Such amorphous (glassy and non-glassy MOFs) and liquid counterparts can be obtained generally by heating before the decomposition temperature, followed by fast or slow cooling. Herein, the organic ligands remain intact, and the coordination binding between them and metal clusters is partially retained. In contrast, overcoming the decomposition temperature leads to the formation of amorphous materials[16−19] which consist of fully or partially decomposed ligands, carbon, and a wide range of nanoparticles. Herein, no structural integrity and coordination bonds are observed.

The resulting amorphous phases demonstrate highly promising mechanical, catalytic and optical properties,[15,20−23] being nonspecific for their crystalline analogues. Nevertheless, in spite of the great potential of such phases, the dynamics of their transformation and the effect of parent MOF chemistry on the result yet remain unclear. Very recently, Rasmus S.K. Madsen and colleagues[24] investigated the glass formation mechanism in ZIF-62, utilizing ultrahigh-field ^{67}Zn solid-state nuclear magnetic resonance spectroscopy. The authors revealed that the two sites (the less and more distorted tetrahedron $Zn–N_4$) have been transferred into a single tetrahedral site upon melting and vitrification, related to the reconstruction of the Zn–N bond. The melting mechanism for ZIF series has been investigated by F.X. Coudert and colleagues[25] with the use of *in situ* variable temperature X-ray and ex-situ neutron pair distribution function experiments. The authors confirmed that during melting, bond breaking and reorientation between Zn^{2+} and imidazolate occur from the undercoordinated Zn^{2+}, producing the disordered structures. A similar *in situ* X-ray pair distribution function technique has been also utilized to probe the mechanism through which MOFs transform into nanocomposites during pyrolysis.[26] Zhihengyu Chen et al.

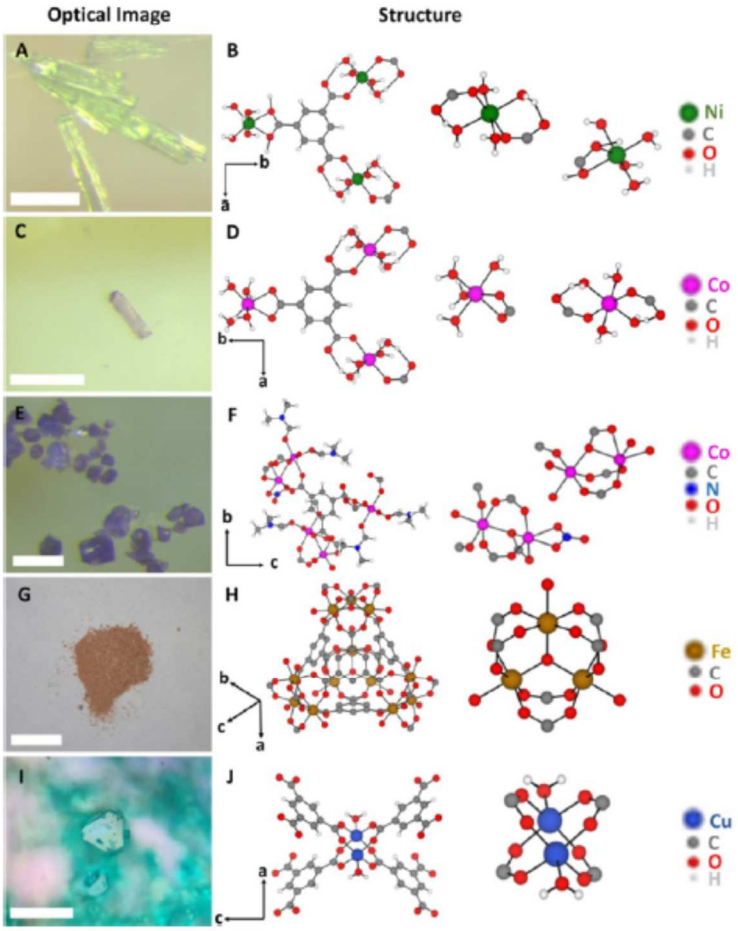

Figure 1. Structure of *M*-BTC compounds. Optical images of the corresponding MOFs: Ni-BTC (A), Co-BTC (C), Co-BTC* (E), Fe-BTC (G), and Cu-BTC (I) with the corresponding scale bars, 200 μm (A,C,E), 1 cm (G), and 20 μm (I). The structure and metallic clusters of the corresponding MOFs: Ni-BTC (B), Co-BTC (D), Co-BTC* (F), Fe-BTC (H), and Cu-BTC (J).

compared a series of bimetallic MOFs with trimeric node different compositions (Fe_3, Fe_2Co, and Fe_2Ni) linked by carboxylate ligands and demonstrated that the resulting nanoparticle structure and chemistry depend on the node chemistry of the parent MOF.

Here, we utilize *in situ* high-resolution transmission electron microscopy (HRTEM)[27−29] to explore the path through which a crystalline MOF single crystal destabilizes and then undergoes the amorphization followed by transformation into MOF-based amorphous nanomaterials. As model MOFs, we consider a series of *M*-BTC (*M*: Cu^{2+}, Ni^{2+}, Co^{2+}, Co^{3+} and Fe^{3+} and BTC: 1,3,5-benzentricarboxylic acid) with an appropriate level of crystallinity of the initial state (especially Ni-BTC and Co-BTC, see Supporting Information, Part I). To avoid the classical equilibrium path of thermal amorphization of MOFs, we turned to a non-thermal way via accelerated 200 kV high-energy electrons with variable flux densities. Intriguingly, this allows us to keep the integrity of the BTC ligand, while destroying the weaker coordination bonds. These have been confirmed by energy dispersive X-ray analysis (EDX) and confocal Raman and photoluminescence (PL) spectroscopy. HRTEM imaging over time with a 100 Hz framing rate (i.e., 0.01 s per micrograph) also made it possible to analyze the formation rates of the amorphous phases and the chemical effect of the parent MOFs; the variation in the topology of metal clusters shifts the rate of formation from 1 to 30 min for an amorphous phase containing an intact BTC ligand and crystalline metal or metal oxide nanoparticles, respectively. We also discovered the dynamics and the nature of the growing nanoparticles on the structural defects with time resolution. Aside from the direct insight into non-thermal solid-to-solid transformation of MOF-based amorphous phases, the research also expands the library of MOF-based nanomaterials for optical applications and contributes to understanding of complex processes of phase transformations in hierarchical solids.[30−32]

■ RESULTS

As the model MOFs, we have synthesized a series of *M*-BTC (*M*: Fe^{3+}, Co^{3+}, Co^{2+}, Ni^{2+}, and Cu^{2+} and BTC: 1,3,5-benzentricarboxylic acid) by a solvothermal method.[33−38] Important is that the variation of metal ions at a fixed ligand allows us to explore the chemistry and topology of the metal cluster of the parent MOF on the dynamics and the composition of resulting amorphous phases. Figure 1 demonstrates the structures of the obtained compounds: Ni-BTC (Figure 1A,B) and Co-BTC (Figure 1C,D) represent similar structures composed of

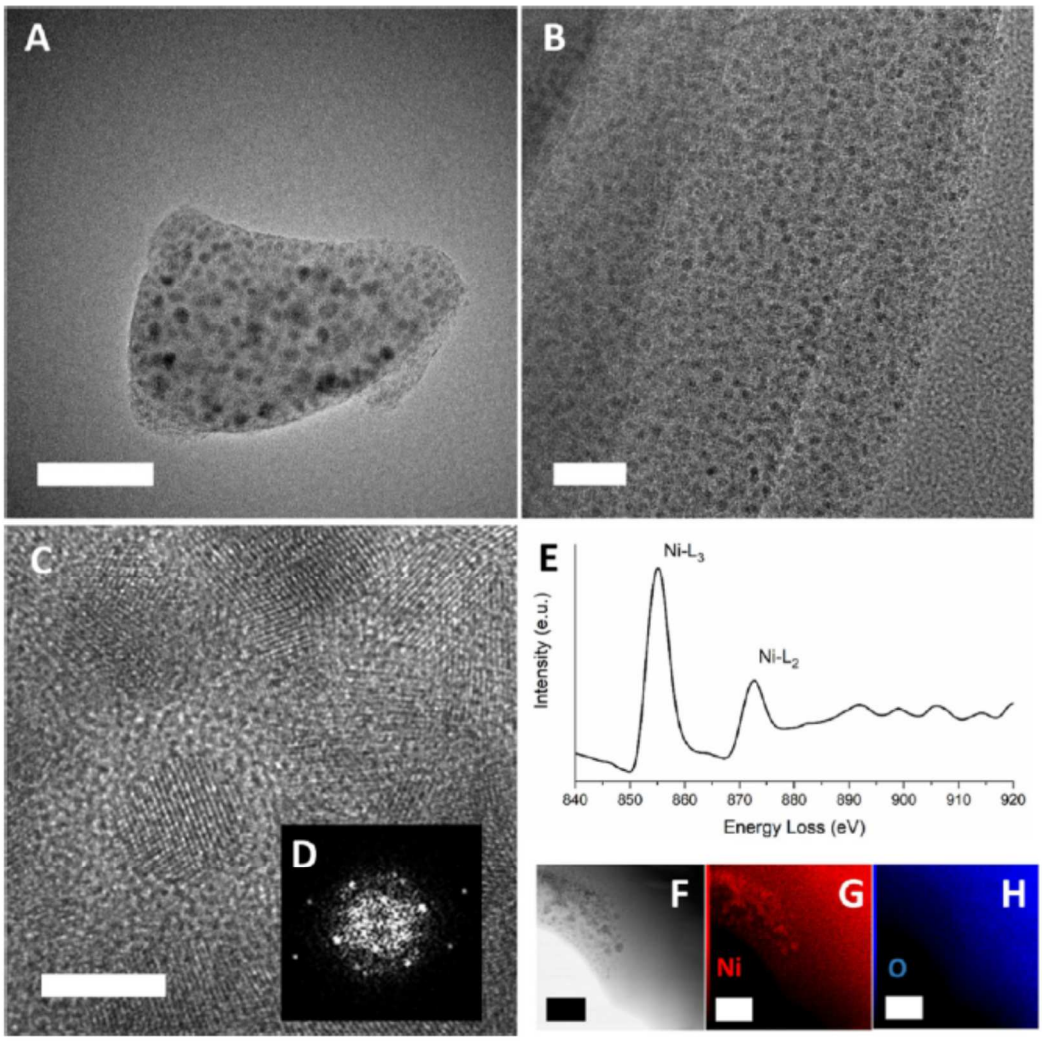

Figure 2. High Resolution TEM analysis of Ni-BTC. (A) Micrograph of the MOF after e-beam exposure. Scale bar, 50 nm. (B,C) Enlarged scale of the resulting nanoparticles immersed inside the organic matrix. Scale bars, 20 nm (B) and 5 nm (C). (D) Fourier transformation of the micrograph (C) confirmed high crystallinity of the obtained nanoparticles. (E) EELS spectrum of the obtained nanoparticles, confirming their metallic (Ni) nature. (F–H) TEM and EDX mapping images of the MOF after e-beam exposure. Scale bar, 100 nm.

$[Ni_3(BTC)_2{\cdot}12H_2O]$ and $[Co_3(BTC)_2{\cdot}12H_2O]$, based on single crystal X-ray diffraction (SCXRD) analysis (see details in the Supporting Information, Tables S1 and S2, Figure S2B). The X-ray data shows that Ni and Co possess separate octahedral positions, and the structure consists of zigzag chains built of two symmetry nonequivalent tetra-aqua M(II) units and BTC ligands. Also, these compounds crystallize in a monoclinic system with a space group of C_2(#5), being isotypic to the structure first obtained by Omar Yaghi and colleagues, and others.[37,39,40] We have also tuned the synthetic parameters (replacement of water by dimethylformamide, DMF, as a solvent, see Experimental Section) to change at least the coordination sphere. As a result, orthorhombic Co-BTC* ($Co_2(BTC)$ (NO_3) × 2DMF) with a space group of $P2_12_12_1$(#19) has been obtained. Based on SCXRD analysis (Table S3), the compound is characterized by two different coordination spheres (Figure 1E,F). The first one is composed of two Co atoms in well-formed and distorted octahedral positions (Figure 1F). The first atom of cobalt bounds with three BTC ligands, two molecules of DMF, and one nitrate ion (NO_3^-). At the second cobalt atom there is one common oxygen atom provided by the BTC ligand. The second sphere is composed of separate Co octahedrons bounded with three BTC ligands and three DMF molecules.

Next, to determine the effect on the coordination sphere through the metal ion change, we have utilized Fe^{3+} to form a cubic MOF ($Fe_3OH(H_2O)_2O[(C_6H_3)\text{-}(CO_2)_3]_2{\cdot}14.5H_2O$) with the $Fd\bar{3}m$(#225) space group referring to ref 41. The obtained powder XRD data (PXRD, Figure S2A) correlate well with that of single crystal analysis from ref 41, confirming that three Fe atoms have four octahedral positions with a common oxygen atom.[42] All octahedral positions have similar structures and bound with oxygen atoms of BTC ligands (Figure 1G,H). Finally, as a part of M-BTC series (Figures 1I,J, and S1), we have taken into consideration the Cu-BTC compound (i.e., $[Cu_3(BTC)_2{\cdot}3H_2O]$ or HKUST-1 purchased from Sigma-

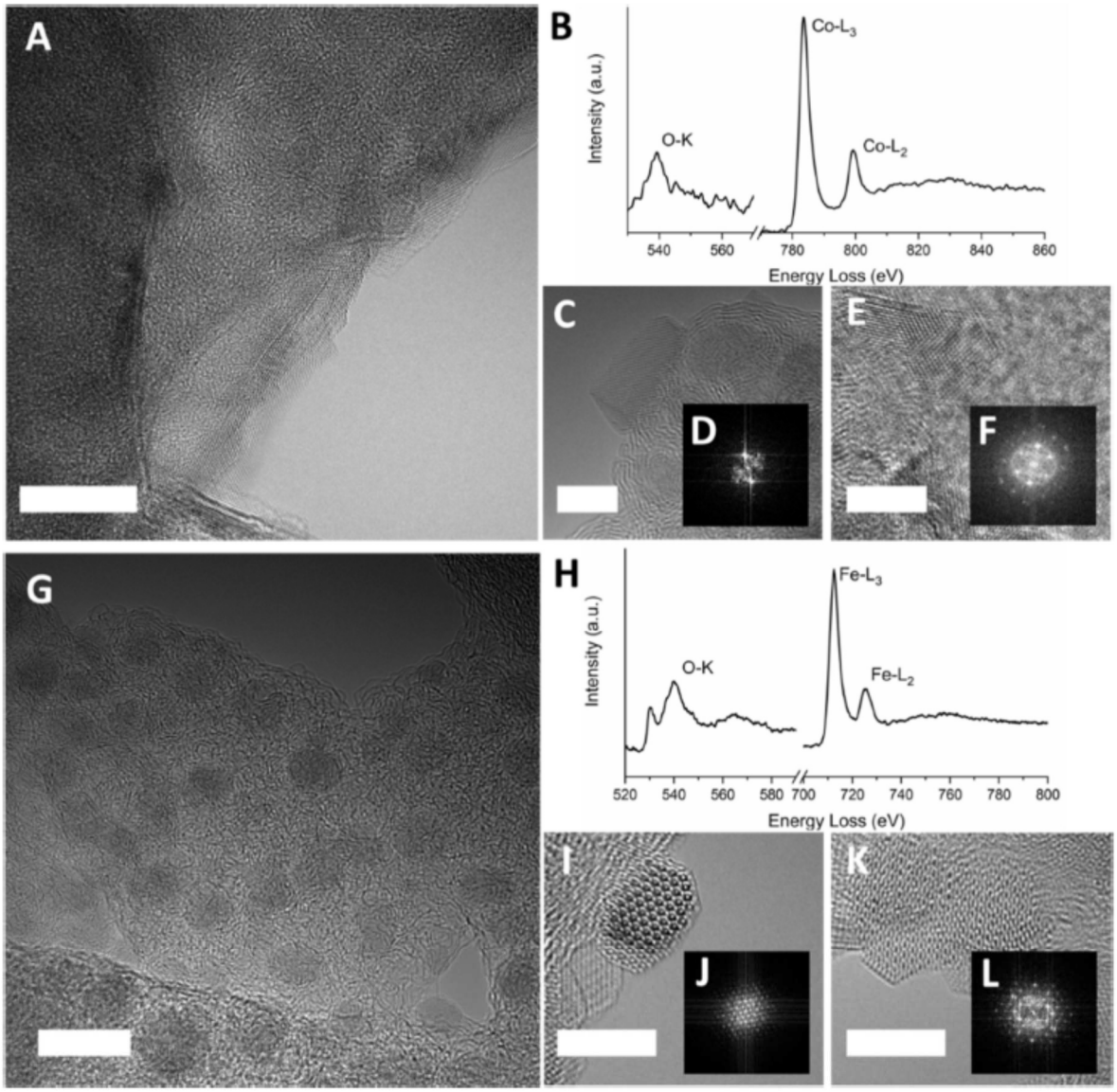

Figure 3. High Resolution TEM analysis of Co-BTC* and Fe-BTC. Structural and chemical analysis of Co-BTC* (A–F) and Fe-BTC (G–L) after e-beam exposure. (A,C,E) HRTEM micrographs of Co-BTC* after e-beam exposure, revealing the highly crystalline nanoparticles inside the organic matrix. Scale bar, 10 nm (A) and 5 nm (C, E). (B) EELS spectrum of the obtained nanoparticles, confirming their oxide state. (D,F) Fourier transformations of the micrographs (C,E) confirmed high crystallinity of the obtained oxide nanoparticles. (G,I,K) HRTEM micrographs of Fe-BTC after e-beam exposure, revealing the highly crystalline nanoparticles inside the organic matrix. Scale bars, 10 nm (G) and 5 nm (I,K). (H) EELS spectrum of the obtained nanoparticles, confirming their oxide state. (J,L) Fourier transformations of the micrographs (I,K) confirmed high crystallinity of the obtained oxide nanoparticles.

Aldrich), characterized by a face-centered cubic structure having an intersecting three-dimensional system in which Cu has two separate elongated rectangular pyramidic positions. The structure of Cu-BTC consists of two Cu atoms, each of which forms four bonds with the oxygen from the BTC ligand and one from the water molecule. This compound has been recently investigated by us in the structural transformation,[43] amorphization, and nanocomposite formation.[44]

We then analyzed solid-to-solid transformations of single crystals of MOFs in the vacuum chamber of a TEM microscope (MET, JEOL ACCEL ARM 200F) under the electronic beam of the varied density from 50 to 120 pA cm^{-2}, accelerated by 200 kV. The initial single crystals of MOFs, when placed in the chamber, demonstrated instant amorphization (Figures S3–S7) with the preservation of coordination bonds and the ligand itself, confirmed by Raman and PL spectroscopy (see the model compounds of Ni-BTC and Co-BTC in Figures S26 and S28, respectively). Herein, the switching to a high-resolution mode with an increase in the electron density turned the e-beam into a tool for destabilization of the parent structure due to energy transfer from incident accelerated electrons to valence electrons in MOFs. To track this inner dynamics, HRTEM micrographs

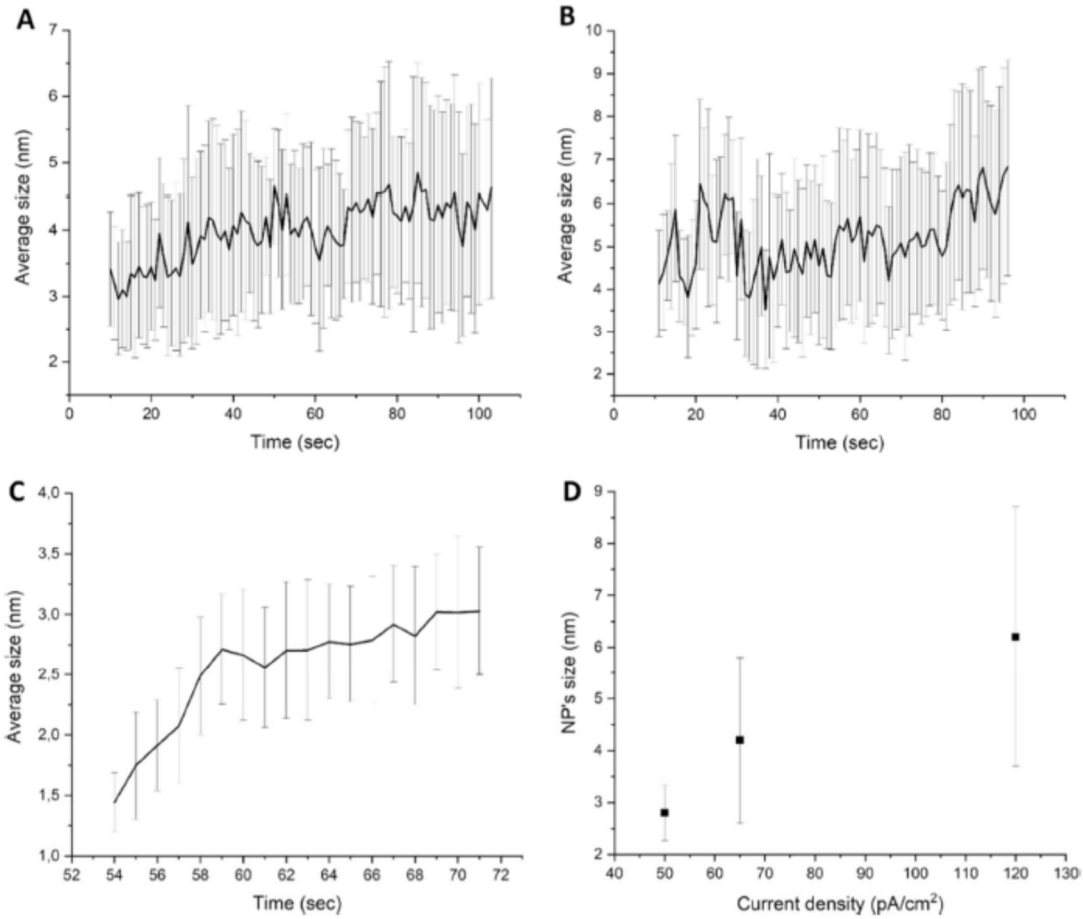

Figure 4. Dynamics of Ni nanoparticle growth. (A,B) Evolution of the average diameter of Ni nanoparticles growing due to Ni-BNC e-beam exposure at 65 pA cm^{-2}, 200 kV (A), and 120 pA cm^{-2}, 200 kV (B). (C) Evolution of the average diameter of Ni nanoparticles growing at −110 °C, 50 pA cm^{-2}, 200 kV. (D) Dependence of the average diameters of Ni nanoparticles on the current density, achieved in 100 s after e-beam exposure.

with a 100 Hz framing rate have been recorded over the full time of the MOF structure transformation (up to 30 min, see Experimental Section).

Figures 2 and 3 summarize the results for non-thermal high-energy electron induced amorphization of the MOF series. As one can see, Ni-BTC demonstrates fast (dozens of seconds, Figure S8) solid-to-solid transformations into a nanomaterial which is composed of crystalline nanoparticles inside an organic matrix (Figure 2A−D). Concerning the nanoparticles, electron energy loss spectroscopy (EELS) revealed their metallic nature via L-edges (L3 and L2) for nickel centered at ∼855 and ∼872 eV (Figure 2E), respectively.[45] In addition, Fourier analysis of HRTEM micrographs (Figure S22) and EDX mapping also confirmed the localization of nickel atoms inside the matrix, while oxygen was distributed throughout the entire volume (Figure 2F−H).

Demonstrating the same topology, Co-BTC also undergoes fast amorphization (Figure S9) with the following crystallization of cobalt nanoparticles inside the organic matrix (Figures S10 A−D and S11). EELS measurements confirmed the metallic nature of the nanoparticles: Co L-edges (L3 and L2) centered at ∼780 and ∼795 eV (Figure S10E), respectively, have been detected without the presence of oxygen.[42] Fourier analysis (Figure S23) and EDX mapping also revealed an accumulation of cobalt atoms, while the oxygen was homogeneously distributed over the volume of the matrix (Figure S10 F−H).

We have recently confirmed the same behavior for Cu-BTC:[44] the formation of metallic Cu particles inside the organic matrix. Herein, a long exposition (app. 2 min) of such compounds under e-beam leads to metallic nanoparticle growth and agglomeration followed by sufficient mechanical deformation of the organic matrix (Movie S1).

In contrast, Co-BTC* (Figure 3A−F) and Fe-BTC (Figure 3G−L) exhibit 30 times slower process (Figure S12) of transformation into nanomaterials with crystalline nanoparticles (Figure 3C−L, Figures S13−S18) immersed in the organic matrix. For the nanoparticles inside the Co-BTC* precursor, EELS measurements revealed two cobalt L-edges, centered at ∼783 and ∼799 eV, and O−K-edges at ∼530 and ∼540 eV for Co-BTC* (Figure 3B). Comparing the obtained data with well-known EELS spectra for the stable cobalt oxide states,[46] we have revealed the following: For metallic cobalt, the L-edges are around 781 (L3) and 796.5 eV (L2), respectively, without any appearances of the oxygen K-edge in the range of 520−580 eV. Herein, the CoO state is characterized with cobalt L-edges at 785.5 (L3) and 801.5 eV (L2), respectively, while Co_3O_4

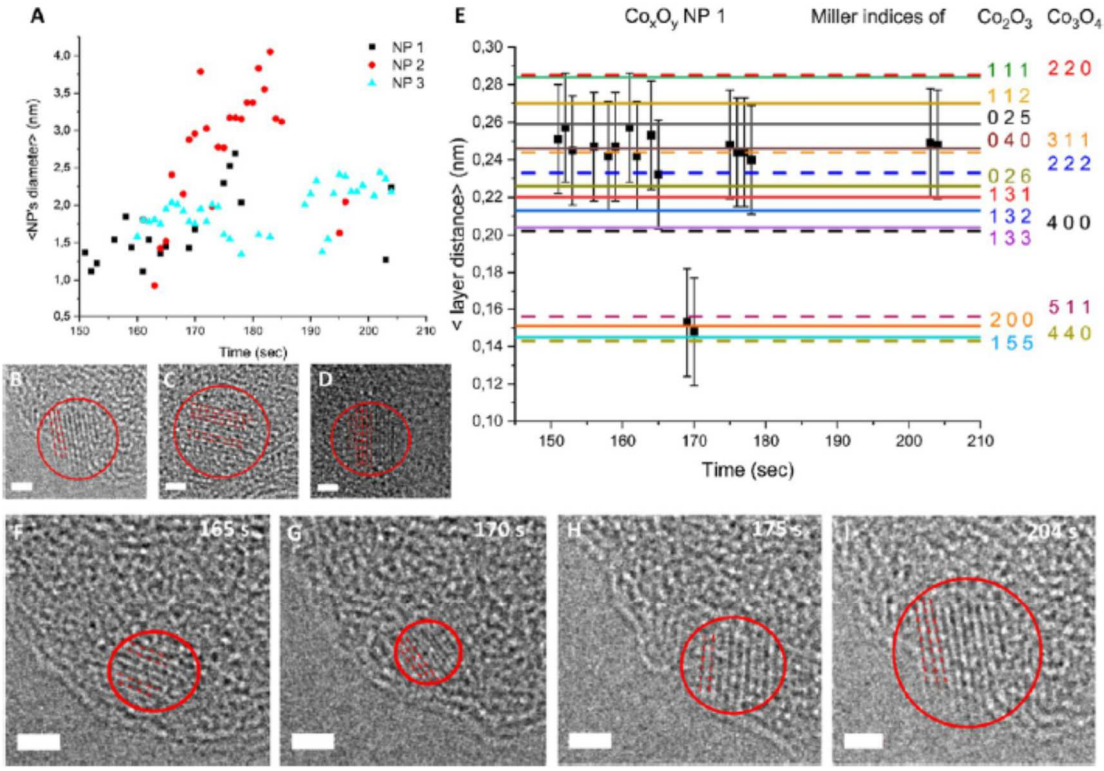

Figure 5. Dynamics of Co_xO_y nanoparticle growth. (A) The evolution of the average diameter of different Co_xO_y nanoparticles (NP1 to NP3) growing inside Co-BTC* during e-beam exposure (100 pA cm^{-2}, 200 kV). (B,C,D) HRTEM micrographs of the nanoparticles NP1 (B), NP2 (C), and NP3 (D). Scale bar, 1 nm. (E) Evolution of the average lattice distance of the nanoparticle NP1 over time, compared with the Miller indices of the bulk Co_2O_3 (solid lines) and Co_3O_4 (dashed lines). (F−I) HRTEM microphotographs of the Co_xO_y nanoparticles, confirming their rotation during solid-to-solid transformation. Scale bar, 1 nm.

exhibits cobalt L-edges near 787 (L3) and 802.5 eV (L2), respectively. The O−K edge range of 520−580 eV for both oxide forms (CoO and Co_3O_4) exhibits three peaks from 530 to 545 eV. It is also important to note that the L3/L2 ratio in our case mismatches with that of the well-known cobalt oxide states. Nevertheless, Fourier analysis of the corresponding nanoparticles reports on the correlation of the obtained Co oxide with the Co_3O_4 state (Figure S24). Thus, these contradictory results allow us to definitely confirm the metal oxide state of the nanoparticles, rather than the exact oxide state of Co (i.e., preferably Co^{3+} or Co^{2+}).

For the nanoparticles inside the Fe-BTC precursor, EELS measurements revealed that L-edges of iron appeared at 713 and 725 eV, and the O−K-edge range has been observed at ∼531 and ∼540 eV with a hump at 565 eV (Figure 3H). It means that the obtained nanoparticles inside the organic matrix possess the Fe^{3+} oxide state, which correlates with the metal state of the parent MOF and the literature.[47] Fourier analysis also supports the Fe_3O_4 state of the resulting nanoparticles (Figure S25).

Next, to reveal the dynamics (with a 0.01 s time resolution) of internal structural transformation and, in particular, the formation of nanomaterials from the amorphous phase, we recorded and statistically processed more than 6×10^5 HRTEM micrographs for the model Ni-, Co-, and Fe-BTC (see Experimental Section). As representative and opposite compounds, we consider below Ni-BTC (Figure 4) and Co-BTC* (Figure 5) in detail.

Upon 65 pA cm^{-2} of electron beam current density, we revealed the growth of Ni nanoparticle in 10 s, once the e-beam switched on (Figure 4A). The 4.2 nm average size of the nanoparticles has been achieved in 100 s. The increase of the current density to 120 pA cm^{-2} yields the larger nanoparticles with an average diameter of ∼6.3 nm in 100 s (Figure 4B). Since the temperature plays a crucial role for the atom diffusion during the nanoparticle growth, we also performed HRTEM analysis at −110 °C (Figure 4C). As one can see, 50 pA cm^{-2} of the current density leads to significant shift of the growth process in time (54 s once the e-beam switched on). Nevertheless, the growth of Ni nanoparticles under the low temperature conditions allowed one to achieve a diameter of ∼3 nm in 70 s. A similar behavior of the nanomaterial formation has also been detected recently for the Cu-BTC[44] and here for Co-BTC (Figure S11): 4 nm average diameter for Co nanoparticles has been achieved in 68 s (at room temperature, 120 pA cm^{-2}).

It should be noted that due to the instrumental limits of the HRTEM approach, we were able to detect the growth process of the nanoparticles with a minimum diameter of 1.5 nm for Ni and Co, instead of detecting the nucleation process.[29] Nevertheless, these are in a good agreement with the recently reported minimal diameters of ∼1 nm Ni[48] and ∼2 nm Co[49,50] nanocrystallites. Moreover, we have revealed that the growth of metal nanoparticles (Ni or Co) inside the organic matrix is accompanied by (i) a constant lattice parameters (within the metrical error, Figure S21A), (ii) constant lattice orientation in

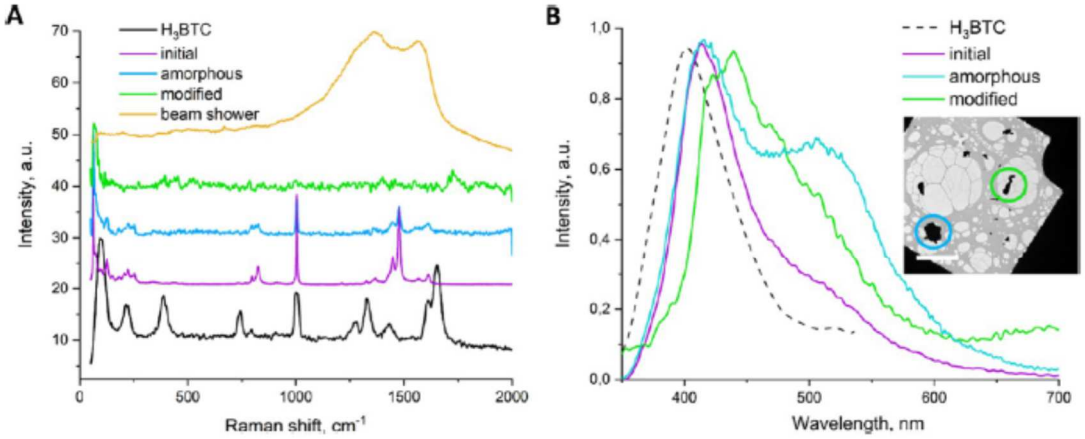

Figure 6. Optical analysis of solid-to-solid transformation of Ni-BTC amorphous phases. (A) Raman spectra of initial, amorphous, and e-beam-modified Ni-BTC compared with those of ligand powder (H_3BTC) and decomposed Ni-BTC by e-beam shower. (B) PL spectra of initial, amorphous, and e-beam-modified Ni-BTC compared with ligand powder (H_3BTC). Inset: Image of a single MOF Ni-BTC on the TEM grid. Scale bar, 200 μm.

space (Figure S21B–E), and (iii) the constant spatial position of the nanoparticle over time (Figure S9). This, in turn, indicates the nucleation and growth of such nanoparticles on the fixed positions inside the MOF precursors.

The more complicated dynamics has been revealed for Co-BTC* (Figure 5). First, during the growth process (up to 4 min), the nanoparticles have appeared at the unstable mode inside the organic matrix. This is characterized by chaotic changes of their size, shape,[51] and position (Figure 5A). For instance, the nanoparticles could disappear and appear again on the same place: the nanoparticle NP1 disappeared 4 times during the observation at ~166, ~171, ~179 s, and at ~205 s (Figure 5E); the nanoparticle NP2 disappeared twice at 186 and 197 s (Figure S19); and the nanoparticle NP3 disappeared three times at 177, 185, and 205 s (Figure S20). Second, we detected the evolution of the layer distances during the growth process. Indeed, the nanoparticle NP1 shows the constant layer distances of ~0.230–0.260 nm during 15 s, and then, we detected ~0.150 nm in 5 s, ~0.240–0.250 nm in 10 s, and ~0.250 nm in 38 s (Figure 5E). The nanoparticles NP2 and NP3 also demonstrate the same behavior (Figures S19 and S20): jump from ~0.210–0.215 nm to ~0.247–0.257 nm in 10 s; jump from ~0.208–0.215 to ~0.175–0.177 in 2 s and to ~0.210–0.220 in 5 s. These observations lead us to conclude that, in contrast to their metal analogues, the growth of metal oxide nanoparticles is accompanied with their mechanical rotation for several seconds (Figure 5F–I). A similar effect has also been detected by HRTEM for iron oxyhydroxide nanoparticles in solution.[52]

In addition, based on the observed layer distances for cobalt oxide nanoparticles (Figures 5E andS19A, S20A), we were able to compare these distances with those of known oxide forms of cobalt (CoO, Co_2O_3, and Co_3O_4) determined by crystallographic methods and calculations.[53,54] Based on the lower Miller indices, we have revealed that the obtained nanoparticles possess the values closer to those of the less stable Co_2O_3 form and/or more stable Co_3O_4 (i.e., the form of $CoO{\cdot}Co_2O_3$). Thus, omitting the exact composition, we nevertheless confirm again the oxide nature of the nanoparticles obtained from the Co-BTC* precursor.

Finally, to shed light on the nature of the organic matrix obtained upon electron induced transformation of MOF precursors, we have analyzed the initial (after the solvothermal synthesis), amorphous (after placement inside the TEM chamber), and e-beam modified MOFs by confocal Raman spectroscopy and PL measurement (Figure 6 for model Ni-BTC and Figure S28 for Co-BTC). As one can see, Raman spectra for the ligand powder (Figure 6A) and its solution in DMF (Figure S26) correlate with that of the initial crystal over the 700–1800 cm^{-1} range, corresponding to the vibrations of the organic part (Tables S4 and S5). Also, the coordination bonds and vibrations of the metal cluster over 200–250 cm^{-1} have been detected for the MOF crystals (see Supporting Information, Part III). Amorphization inside the TEM chamber and further e-beam modification lead to the drop of the intensity of all Raman modes and then to their disappearance, especially the peaks over 200–250 cm^{-1}. Moreover, the original color of the Ni-BTC MOF has been preserved after the e-beam modification, as shown in Figure S26B. It is intriguing that we observed the ligand decomposition only at a sufficient increased dose of the electron exposure (e-beam shower regime in TEM) through the appearance of carbon modes at 1320 and 1570 cm^{-1} (Figure 6A). PL measurements also confirm the amorphization of the single MOF crystal through the red shift of the PL spectra[55] and the growth of a broad band at 500 nm apparently, corresponding to a loss of the crystal order. Correlating with the Raman data and the fact of the nanoparticle formation, the PL signal from the representative e-beam-modified Ni-BTC and Co-BTC confirms again the ligand intact state, while the coordination bonds disappear. In addition, we have compared the PL signal from e-beam-modified Ni-BTC as prepared and hold for 4 months at ambient conditions (Figure S26B). As one can see, the nanomaterial demonstrates a similar PL signal with a slightly disturbed shape possible due to ongoing amorphization, in a good agreement with optical behavior of MOF-based glasses.[56]

■ DISCUSSION

Since we have observed significant differences in the dynamics of solid-to-solid transformation, and the chemical composition of the resulting amorphous solids, we can conclude that the "chemical prehistory" of the initial MOF (generally, the metal clusters) determines the path of the transformation.[26,57–59] In fact, all MOFs discussed within the paper (Figure 1) can be organized into two groups, based on the absence or presence of the M–O–M bond (*M*: metal ion). Thus, the first group

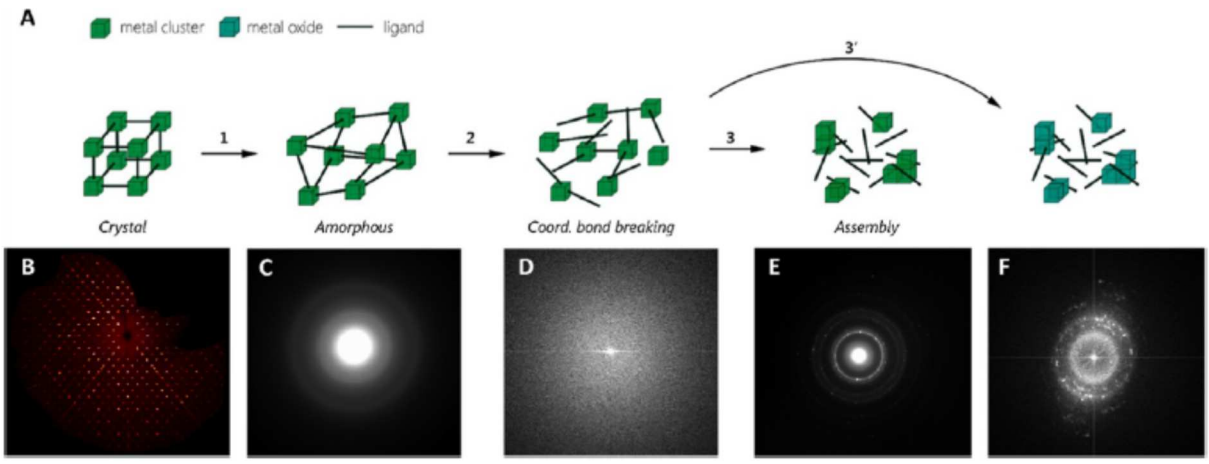

Figure 7. Path of solid-to-solid transformation of MOF amorphous phases. (A) Schematic diagram of evolution of the MOF (*M*-BTC) structure: (1) amorphization in a vacuum chamber of the TEM microscope; (2) e-beam exposure that triggers the processes of coordination bond breaking and subsequent (3) self-assembly of metals in 1 min and (3′) metal oxides in 30 min. (B−F) Corresponding diffraction images demonstrating the evolution of crystallinity and appearance of different phases during e-beam exposure.

contains Ni-BTC, Co-BTC, and Cu-BTC, in which metal−oxygen polyhedrons are situated separately from each other without joint vertices. The second group contains Co-BTC* and Fe-BTC, respectively, in which metal−oxygen polyhedrons have at least one joint vertex occupied by an oxygen.[60] Most probably, electron beam action can break the bonds between the metal ion and ligand but not the bonds formed by joint oxygen in the metallic cluster. This feature leads to a remarkable difference in the e-beam treatment products of MOFs belonging to the first group (metallic Ni, Co, and Cu nanoparticles) and to the second one (Co and Fe oxide nanoparticles). To clarify this situation, we have estimated the bond energies by quantum chemical calculations for the representative Co-BTC and Co-BTC* compounds (see Supporting Information, Part IV). We have found that the complex topology of the metallic cluster in Co-BTC* (Figure 1F) provides ∼40% higher bond energy of Co ions with oxygen in specific positions, compared to other Co−O bonds in Co-BTC* (Figure S31 and Table S6). However, the strongest Co−O bonds in Co-BTC are 20% weaker compared to those of Co-BTC* and hence easier to break. This possibly brings us to the conclusion on the effect of the metal cluster on the resulting metal or metal oxide chemistry of the nanoparticles during the structural transformation.

The ligand integrity is also an important point in our case. In contrast to pyrolysis of MOFs, when the structure itself and the organics undergo thermally stimulated decomposition to carbon, thus forming MOF derivatives,[16−19] we have detected for the first time the formation of the solid amorphous nanomaterial based on intact ligands and crystalline metal or metal-oxide nanoparticles. Following the established terminology,[11,15] we are not able to designate a new amorphous solid as a glassy or an amorphous MOF. This is due to the loss of coordination bonding, which is then accompanied by the growth of the nanoparticles. Nevertheless, the ligand integrity, confirmed indirectly by optical spectroscopy and EDX, brings us to the conclusion on a specific amorphous phase of solid obtained from MOF precursors. Thus, this complements the list of new MOF-based phases in the gap between glassy/amorphous MOFs and their derivatives.[61]

The next issue is the dynamics of the solid-to-solid transformation and the nanoparticle growth (Figure 7), demonstrating a 30-fold change for representative Co-BTC and Co-BTC* compounds. We assume that the rate of amorphization of the framework in the TEM chamber and non-thermal destruction of its coordination bonds under the action of the e-beam depends on the chemistry and the level of structural rigidity of the MOF. Nevertheless, these processes should occur before (or partially overlap with) the nucleation and the growth of the nanoparticles. Thus, a 30-fold change in the rate of the transformation of the MOF into an amorphous organic matrix with metal or metal oxide nanoparticles should be directly related to complex processes of the nanoparticle nucleation and growth on structural inhomogeneities or relatively freely in the volume of the MOF precursor.[52] The dynamics of such processes is determined by the number of reagents (metal or metal and oxygen), their energy favorable ordering, diffusion and ripening of atoms in two-dimensional or three-dimensional space, and concomitant coalescence (if it's possible).[30−32,44,62,63] Observing more complex dynamics of Co and Fe oxide growth and a larger size of their nucleus, we speculate that this leads to a prolongation of the transformation process for Co-BTC* and Fe-BTC. Also, since the dynamics depends on the conditions (i.e., cooling in Figure 4C) and mode of their launch, we have analyzed the possibility of the effect on the growth rate of metallic nanoparticles inside Ni-BTC and Co-BTC precursors, exhibiting fast solid-to-solid transformation. For this, an electron beam accelerated by 20 kV in a chamber of a scanning electron microscope (FEI Quantum Inspect S) has been used. Surprisingly, a 10-fold decrease in the acceleration potential led to unchanged Raman spectra for MOFs, even after 1 h of exposure (Figure S29), confirming the integrity of the ligand, the metal cluster, and the coordination bonds between them.

Finally, with intensive development of the technology of electron lithography of polymers[64] and MOFs,[65] there is growing interest in materials whose structural and functional properties can be changed locally by an electron beam.[66] This opens up the prospect of using MOFs as the key layers of complex structures obtained precisely via high-tech lithography.

CONCLUSIONS

Utilizing *in situ* high-resolution transmission electron microscopy with 0.01 s time resolution, we have explored non-thermal (electron induced) amorphization of MOF single crystals followed by transformation into new amorphous MOF-based nanomaterials. The analysis of a series of *M*-BTC (*M*: Fe^{3+}, Co^{3+}, Co^{2+}, Ni^{2+}, and Cu^{2+}; BTC: 1,3,5-benzentricarboxylic acid) allowed us to reveal experimentally and numerically that the topology of a metal cluster determines the rate of formation (from 1 to 30 min) and the chemistry of the resulting phases containing an intact BTC ligand and metal or metal oxide nanoparticles. Confocal Raman and photoluminescence spectroscopy further confirm the integrity of the BTC ligand and coordination bond breaking, admitting us to claim specifically the new form of amorphous MOFs. While high-resolution imaging with chemical and structural analysis over time allowed for tracking the dynamics of solid-to-solid transformations and explore the mechanical mobility of growing crystalline nanoparticles, depending on their chemical composition. Given the established non-thermal solid-to-solid transformations of MOFs with a tunable composition into new amorphous phases, these results contribute to understanding of complex processes of phase transformations in hierarchical solids and shed light on rational design of new MOF-based nanomaterials for catalysis, mechanics, and especially optics.[15,20−23,59]

EXPERIMENTAL SECTION

Materials. All materials including $NiSO_4{\cdot}7H_2O$ (Sigma-Aldrich, ≥99.0%), NaOH (ACS reagent, ≥97%), $Co(NO_3)_2{\cdot}6H_2O$ (ACS reagent, ≥98%), $Fe(NO_3)_3{\cdot}9H_2O$ (ACS reagent, ≥98%), 1,3,5-benzenetricarboxylic acid (Sigma-Aldrich, Trimesic acid (H_3BTC), 95%), dimethylformamide (ACS reagent, ≥99.8%), and isopropanol (ACS reagent, ≥99.5%) were used in all syntheses. HKUST-1 (CCDC 943008) (Basolite C 300) has been purchased from Sigma-Aldrich.

MOF Synthesis. Ni-BTC (CCDC 2128682 and the related structures CCDC 1274034 and CCDC 738061) single-crystals were synthesized using a solvothermal method.[33,34] Two initial precursors, $NiSO_4{\cdot}7H_2O$ (2.577 mmol) and 1,3,5-benzenetricarboxylic acid (1.718 mmol), were dissolved separately in 15 mL of distilled water and 15 mL of dimethylformamide, respectively, under ultrasound, using the BANDELIN SONOPLUS HD 2070.2 ultrasonic homogenizer for 2 min at 50% of power and room temperature. Two obtained solutions of precursors were poured together in a heat-resistance SIMAX bottle, and 30 mL of the mixture was placed in an oven at 110 °C for 24 h. Then, the bottle of the final mixture was cooled to room temperature. The resultant green crystals of Ni-BTC were washed three times and stored in the mixed solvent of dimethylformamide/water (1:1 vol %).

Co-BTC (CCDC 2128895 and the related structures CCDC 1274034 and CCDC 1952653) single-crystals were synthesized using a "green" water-based procedure at room temperature.[35] A solution of 0.0125 M Na_3BTC was prepared by dissolving 3.75 mmol of NaOH and 1.25 mmol of 1,3,5-benzenetricarboxylic acid in 100 mL of distilled water under vigorous stirring. 0.1 M $Co(NO_3)_2$ solution was prepared by dissolving 0.01 mol of $Co(NO_3)_2{\cdot}6H_2O$ in 100 mL of distilled water under vigorous stirring. Then, 1.9 mL of 0.1 M $Co(NO_3)_2$ was diluted in 8.1 mL of water and finally in a 10 mL solution of the salt precursor. 10 mL of 0.0125 M Na_3BTC was carefully added by sliding down the walls of the vessel. The final solution was left overnight for crystallization. The pink crystals of Co-BTC were washed three times with water and kept in a solvent.

Co-BTC* (CCDC 2167623) mixed powder with big single-crystals were synthesized using the solvothermal method.[33] Initial precursors $Co(NO_3)_2{\cdot}6H_2O$ (5.154 mmol) and 1,3,5-benzenetricarboxylic acid (3.436 mmol) were dissolved separately in 30 mL of mixed solvents of dimethylformamide and isopropanol with a ratio of 1:1 vol % under ultrasound, using the BANDELIN SONOPLUS HD 2070.2 ultrasonic homogenizer for 2 min at 50% of power and room temperature. Two obtained solutions of precursors were poured together in a heat-resistance SIMAX bottle, and 60 mL of the mixture was placed in an oven at 110 °C for 24 h. Then, the bottle of the final mixture was cooled to room temperature using an ice water bath. The resultant violet particles of Co-BTC* were washed three times and stored in the initial mixed solvent (dimethylformamide/isopropanol (1:1 vol %)).

Fe-BTC (CCDC 640536) powder was synthesized using the hydrothermal method with a reaction between $Fe(NO_3)_3{\cdot}9H_2O$ (9.2 mmol) and 1,3,5-benzenetricarboxylic acid (5.4 mmol) in 40 mL of distilled water.[36] The obtained suspension was heated at 85 °C under constant stirring for 24 h. The resultant orange powder was washed three times and stored in water subsequently.

SCXRD and PXRD Analysis. All MOFs have been analyzed by powder XRD using the Bruker D8 Advance diffractometer in the Bragg−Brentano geometry with monochromated $CuKa_1$ and CoKa wavelengths. The single crystals of Ni-BTC and Co-BTC have been analyzed on the Bruker Kappa Apex II diffractometer equipped with a mirror monochromator and $MoKa_1$ ImS(l = 0.71073 Å). The Apex 3-program package was used for the cell refinements and data reductions. The structure was solved using direct methods and refined with the SHELXL-2013[67] and XSHELL[68] programs. Semi-empirical absorption correction (SADABS) was applied to the data. For Co-BTC*, a suitable crystal was selected and then has been analyzed on the Bruker APEX-II CCD diffractometer. The crystal was kept at 296.15 K during data collection. Using Olex2, the structure was solved with the XT structure solution program using intrinsic phasing and refined with the SHELXL refinement package using least squares minimization.

EDX and EELS Mapping. Due to the high reactivity of MOFs under the electron beam, EDX and EELS maps were recorded after the solid-to-solid transformation. EDX maps were recorded in STEM mode with an 8 cm camera length and using the JEOL Centurio detector (1sr). EELS maps were recorded at 2 cm with a dispersion of 0.025 eV per channel and using the GATAN GIF Quantum spectrometer.

Statistical Analysis of HRTEM Images. Solid-to-solid transformations of a series of *M*-BTC MOFs have been analyzed by HRTEM imaging and video regimes, simultaneously, using the GATAN Oneview camera. For the latter, the series of MOFs have been divided into two sub-groups: Ni-BTC and Co-BTC, possessing fast transformation with simple dynamics; and Co-BTC* and Fe-BTC, possessing slow and complicated dynamics of transformation. The HRTEM video has been recorded with 100 Hz frequency (i.e., 100 HRTEM frames per second) for app. 2 min (for Ni-BTC and Co-BTC) and app. 4 min (for Co-BTC* and Fe-BTC), while HRTEM micrographs have been obtained over the whole period of transformation (up to 30 min) with 0.02 Hz frequency.

For Ni-BTC and Co-BTC, we have analyzed random selections of 100 HRTEM frames of a second during 2 min. As a result, we confirmed the invariability of the nanoparticle size and lattice parameters over a second. Therefore, we decided to analyze the size evolution of the metallic nanoparticles with a 1 s interval (Figure 4). The size estimation has been performed using ImageJ software. Since the initial MOFs were relatively thick, the metallic nanoparticles have appeared as black areas inside the transparent organic matrix in HRTEM micrographs. The analysis of their layer distances has been performed for the nanoparticles on the edges of MOF single crystals (see, for instance, Figures S10 and S11).

For Co-BTC* and Fe-BTC, we have analyzed random selections of 100 HRTEM frames of a second for 4 min. Due to the invariability of the nanoparticle size and lattice parameters over a second for such systems, we considered to analyze the size and lattice parameter evolutions with a 1 s interval. The size estimation of Co_2O_3 has been performed using Gatan Microscopy Suite (GMS) software. The nanoparticles have been selected based on their highly visualized crystalline features such as atomic layers. The diameters of the nanoparticles have also been estimated as the distance between two last atomic layers of chosen nanoparticles. The estimation of the average distances between nanoparticle layers has been performed using the Line Profiles tool of GMS. The obtained layer distances were compared

with low and the most intensive Miller indices of Co_2O_3 and Co_3O_4 (Figure 5E).

Optical Measurements. For optical measurements, single MOF crystals have been placed on the carbon layer of the TEM grid (Figure 6b, inset). The Raman and PL spectra have been measured using the confocal microscope setup; the single crystal has been irradiated by coherent light (He−Ne source with a wavelength of 632.8 nm, 15 mW for Raman and Yb^{3+} femtosecond laser source with a wavelength of 350 nm, 150 fs pulse duration, 80 MHz repetition rate for PL) via a 100*x*/0.9NA objective. The re-emitted light was collected via the same objective and then analyzed using the confocal Raman spectroscopy system HORIBA Labram with 1800 g mm^{-1} diffraction gratings and water-cooling camera ANDOR.

Computational Details. The quantum chemical calculations for Co-BTC* and Co-BTC have been carried out via density functional theory (DFT) using the dispersion-corrected hybrid functional ωB97XD[69] with the help of the Gaussian-09 program package.[70] The standard 6 − 31 + G* basis sets were used for all atoms. The topological analysis of the electron density distribution with the help of the "quantum theory of atoms in molecules" method developed by Bader[71] was performed by using the Multiwfn program, version 3.7.[72] The Cartesian atomic coordinates for model structures Co-BTC* and Co-BTC are presented in Supporting Information.

■ ACKNOWLEDGMENTS

V.A.M. and Y.A.M. acknowledge the financial support from the Russian Science Foundation (Grant numb. 19-79-10241), "Metchnikov" and "Ostrogradski" Program of the French Embassy in Russia, Scholarship of President of the Russian Federation to study abroad, and Russian Foundation for Basic Research (Grant numb. 20-33-90318). S.S. acknowledges the financial support by the Government of the Russian Federation through the ITMO Fellowship and Professorship Program, and the Russian Science Foundation (Grant numb. 22-23-00738). A.S.N. acknowledges the financial support from the RUDN University Strategic Academic Leadership Program.

■ REFERENCES

(1) Mason, J. A.; Oktawiec, J.; Taylor, M. K.; Hudson, M. R.; Rodriguez, J.; Bachman, J. E.; Gonzalez, M. I.; Cervellino, A.; Guagliardi, A.; Brown, C. M.; Llewellyn, P. L.; Masciocchi, N.; Long, J. R. Methane storage in flexible metal-organic frameworks with intrinsic thermal management. *Nature* **2015**, *527*, 357−361.

(2) Rodenas, T.; Luz, I.; Prieto, G.; Seoane, B.; Miro, H.; Corma, A.; Kapteijn, F.; Llabrés i Xamena, F. X.; Gascon, J. Metal−organic framework nanosheets in polymer composite materials for gas separation. *Nat. Mater.* **2014**, *14*, 48−55.

(3) Liu, J.; Wöll, C. Surface-supported metal-organic framework thin films: Fabrication methods, applications, and challenges. *Chem. Soc. Rev.* **2017**, *46*, 5730−5770.

(4) Stavila, V.; Talin, A. A.; Allendorf, M. D. MOF-based electronic and opto-electronic devices. *Chem. Soc. Rev.* **2014**, *43*, 5994−6010.

(5) Kulachenkov, N.; Haar, Q.; Shipilovskikh, S.; Yankin, A.; Pierson, J.-F.; Nominé, A.; Milichko, V. A. MOF-Based Sustainable Memory Devices. *Adv. Funct. Mater.* **2022**, *32*, 2107949.

(6) Li, Z.-G.; Li, K.; Dong, L.-Y.; Guo, T.-M.; Azeem, M.; Li, W.; Bu, X.-H. Acoustic Properties of Metal-Organic Frameworks. *Research* **2021**, *2021*, 9850151.

■ AUTHOR INFORMATION

Corresponding Author

Valentin A. Milichko − *School of Physics and Engineering, ITMO University, St. Petersburg 197101, Russia; Institut Jean Lamour, Universite de Lorraine, UMR CNRS 7198, Nancy 54011, France;* orcid.org/0000-0002-8461-0804; Email: v.milichko@metalab.ifmo.ru

Authors

Yuri A. Mezenov − *School of Physics and Engineering, ITMO University, St. Petersburg 197101, Russia*

Stephanie Bruyere − *Institut Jean Lamour, Universite de Lorraine, UMR CNRS 7198, Nancy 54011, France*

Andrei Krasilin − *Ioffe Institute, St. Petersburg 194021, Russia;* orcid.org/0000-0002-3938-3024

Ekaterina Khrapova − *Ioffe Institute, St. Petersburg 194021, Russia*

Semyon V. Bachinin − *School of Physics and Engineering, ITMO University, St. Petersburg 197101, Russia*

Pavel V. Alekseevskiy − *School of Physics and Engineering, ITMO University, St. Petersburg 197101, Russia*

Sergei Shipiloskikh − *School of Physics and Engineering, ITMO University, St. Petersburg 197101, Russia*

Pascal Boulet − *Institut Jean Lamour, Universite de Lorraine, UMR CNRS 7198, Nancy 54011, France;* orcid.org/0000-0003-0684-4397

Sebastien Hupont − *Institut Jean Lamour, Universite de Lorraine, UMR CNRS 7198, Nancy 54011, France*

Alexandre Nomine − *Institut Jean Lamour, Universite de Lorraine, UMR CNRS 7198, Nancy 54011, France*

Brigitte Vigolo − *Institut Jean Lamour, Universite de Lorraine, UMR CNRS 7198, Nancy 54011, France;* orcid.org/0000-0002-1463-0121

Alexander S. Novikov − *Institute of Chemistry, Saint Petersburg State University, St. Petersburg 198504, Russia; Peoples' Friendship University of Russia (RUDN University), Moscow 117198, Russia;* orcid.org/0000-0001-9913-5324

Thierry Belmonte − *Institut Jean Lamour, Universite de Lorraine, UMR CNRS 7198, Nancy 54011, France*

Complete contact information is available at: https://pubs.acs.org/10.1021/acs.inorgchem.2c01978

Author Contributions

[#]Y.A.M. and S.B. contributed equally to this work.

Notes

The authors declare no competing financial interest.

(7) Evans, A. M.; Giri, A.; Sangwan, V. K.; Xun, S.; Bartnof, M.; Torres-Castanedo, C. G.; Balch, H. B.; Rahn, M. S.; Bradshaw, N. P.; Vitaku, E.; Burke, D. W.; Li, H.; Bedzyk, M. J.; Wang, F.; Brédas, J.-L.; Malen, J. A.; McGaughey, A. J. H.; Hersam, M. C.; Dichtel, W. R.; Hopkins, P. E. Thermally conductive ultra-low-k dielectric layers based on two-dimensional covalent organic frameworks. *Nat. Mater.* **2021**, *20*, 1142−1148.

(8) Lv, Y.; Xiong, Z.; Dong, H.; Wei, C.; Yang, Y.; Ren, A.; Yao, Z.; Li, Y.; Xiang, S.; Zhang, Z.; Zhao, Y. S. Pure Metal−Organic Framework Microlasers with Controlled Cavity Shapes. *Nano Lett.* **2020**, *20*, 2020−2025.

(9) Fujie, K.; Ikeda, R.; Otsubo, K.; Yamada, T.; Kitagawa, H. Lithium Ion Diffusion in a Metal−Organic Framework Mediated by an Ionic Liquid. *Chem. Mater.* **2015**, *27*, 7355−7361.

(10) Son, H.-J.; Jin, S.; Patwardhan, S.; Wezenberg, S. J.; Jeong, N. C.; So, M.; Wilmer, C. E.; Sarjeant, A. A.; Schatz, G. C.; Snurr, R. Q.; Farha, O. K.; Wiederrecht, G. P.; Hupp, J. T. Light-Harvesting and Ultrafast Energy Migration in Porphyrin-Based Metal−Organic Frameworks. *J. Am. Chem. Soc.* **2013**, *135*, 862−869.

(11) Bennett, T. D.; Horike, S. Liquid, glass and amorphous solid states of coordination polymers and metal−organic frameworks. *Nat. Rev. Mater.* **2018**, *3*, 431−440.

(12) Widmer, R. N.; Lampronti, G. I.; Anzellini, S.; Gaillac, R.; Farsang, S.; Zhou, C.; Belenguer, A. M.; Wilson, C. W.; Palmer, H.; Kleppe, A. K.; Wharmby, M. T.; Yu, X.; Cohen, S. M.; Telfer, S. G.; Redfern, S. A. T.; Coudert, F.-X.; MacLeod, S. G.; Bennett, T. D. Pressure promoted low-temperature melting of metal−organic frameworks. *Nat. Mater.* **2019**, *18*, 370−376.

(13) Shaw, B. K.; Hughes, A. R.; Ducamp, M.; Moss, S.; Debnath, A.; Sapnik, A. F.; Thorne, M. F.; McHugh, L. N.; Pugliese, A.; Keeble, D. S.; Chater, P.; Bermudez-Garcia, J. M.; Moya, X.; Saha, S. K.; Keen, D. A.; Coudert, F.-X.; Blanc, F.; Bennett, T. D. Melting of hybrid organic−inorganic perovskites. *Nat. Chem.* **2021**, *13*, 778−785.

(14) Nozari, V.; Calahoo, C.; Tuffnell, J. M.; Keen, D. A.; Bennett, T. D.; Wondraczek, L. Ionic liquid facilitated melting of the metal-organic framework ZIF-8. *Nat. Commun.* **2021**, *12*, 5703.

(15) Horike, S.; Ma, N.; Fan, Z.; Kosasang, S.; Smedskjaer, M. M. Mechanics, Ionics, and Optics of Metal−Organic Framework and Coordination Polymer Glasses. *Nano Lett.* **2021**, *21*, 6382−6390.

(16) Jagadeesh, R. V.; Murugesan, K.; Alshammari, A. S.; Neumann, H.; Pohl, M.-M.; Radnik, J.; Beller, M. MOF-derived cobalt nanoparticles catalyze a general synthesis of amines. *Science* **2017**, *358*, 326−332.

(17) Indra, A.; Song, T.; Paik, U. Metal Organic Framework Derived Materials: Progress and Prospects for the Energy Conversion and Storage. *Adv. Mater.* **2018**, *30*, 1705146.

(18) Ghosh, S.; Yun, H.; Kumar, P.; Conrad, S.; Tsapatsis, M.; Mkhoyan, K. A. Two Distinct Stages of Structural Modification of ZIF-L MOF under Electron-Beam Irradiation. *Chem. Mater.* **2021**, *33*, 5681−5689.

(19) Mingabudinova, L. R.; Zalogina, A. S.; Krasilin, A. A.; Petrova, M. I.; Trofimov, P.; Mezenov, Y. A.; Ubyivovk, E. V.; Lönnecke, P.; Nominé, A.; Ghanbaja, J.; Belmonte, T.; Milichko, V. A. Laser printing of optically resonant hollow crystalline carbon nanostructures from 1D and 2D metal−organic frameworks. *Nanoscale* **2019**, *11*, 10155−10159.

(20) Hou, J.; Chen, P.; Shukla, A.; Krajnc, A.; Wang, T.; Li, X.; Doasa, R.; Tizei, L. H. G.; Chan, B.; Johnstone, D. N.; Lin, R.; Schülli, T. U.; Martens, I.; Appadoo, D.; Ari, M. S.; Wang, Z.; Wei, T.; Lo, S.-C.; Lu, M.; Li, S.; Namdas, E. B.; Mali, G.; Cheetham, A. K.; Collins, S. M.; Chen, V.; Wang, L.; Bennett, T. D. Liquid-phase sintering of lead halide perovskites and metal-organic framework glasses. *Science* **2021**, *374*, 621−625.

(21) Stepniewska, M.; Januchta, K.; Zhou, C.; Qiao, A.; Smedskjaer, M. M.; Yue, Y. Observation of indentation-induced shear bands in a metal−organic framework glass. *Proc. Natl. Acad. Sci. U.S.A.* **2020**, *117*, 10149−10154.

(22) Widmer, R. N.; Bumstead, A. M.; Jain, M.; Bennett, T. D.; Michler, J. Plasticity of Metal−Organic Framework Glasses. *J. Am. Chem. Soc.* **2021**, *143*, 20717−20724.

(23) Bumstead, A. M.; Pakamorė, I.; Richards, K. D.; Thorne, M. F.; Boyadjieva, S. S.; Castillo-Blas, C.; McHugh, L. N.; Sapnik, A. F.; Keeble, D. S.; Keen, D. A.; Evans, R. C.; Forgan, R. S.; Bennett, T. D. Post-Synthetic Modification of a Metal-Organic Framework Glass. *Chem. Mater.* **2022**, *34*, 2187−2196.

(24) Madsen, R. S. K.; Qiao, A.; Sen, J.; Hung, I.; Chen, K.; Gan, Z.; Sen, S.; Yue, Y. Ultrahigh-field ^{67}Zn NMR reveals short-range disorder in zeolitic imidazolate framework glasses. *Science* **2020**, *367*, 1473−1476.

(25) Gaillac, R.; Pullumbi, P.; Beyer, K. A.; Chapman, K. W.; Keen, D. A.; Bennett, T. D.; Coudert, F.-X. Liquid metal−organic frameworks. *Nat. Mater.* **2017**, *16*, 1149−1154.

(26) Chen, Z.; Chen, Z.; Farha, O. K.; Chapman, K. W. Mechanistic Insights into Nanoparticle Formation from Bimetallic Metal−Organic Frameworks. *J. Am. Chem. Soc.* **2021**, *143*, 8976−8980.

(27) Gong, X.; Gnanasekaran, K.; Chen, Z.; Robison, L.; Wasson, M. C.; Bentz, K. C.; Cohen, S. M.; Farha, O. K.; Gianneschi, N. C. Insights into the Structure and Dynamics of Metal−Organic Frameworks via Transmission Electron Microscopy. *J. Am. Chem. Soc.* **2020**, *142*, 17224−17235.

(28) Choudhary, M. K.; Jain, R.; Rimer, J. D. In situ imaging of two-dimensional surface growth reveals the prevalence and role of defects in zeolite crystallization. *Proc. Natl. Acad. Sci. U.S.A.* **2020**, *117*, 28632−28639.

(29) Liu, X.; Chee, S. W.; Raj, S.; Sawczyk, M.; Král, P.; Mirsaidov, U. Three-step nucleation of metal−organic framework nanocrystals. *Proc. Natl. Acad. Sci. U.S.A.* **2021**, *118*, No. e2008880118.

(30) Anderson, V. J.; Lekkerkerker, H. N. W. Insight into phase transition kinetics from colloid science. *Nature* **2002**, *416*, 811−815.

(31) Peng, Y.; Wang, F.; Wang, Z.; Alsayed, A. M.; Zhang, Z.; Yodh, A. G.; Han, Y. Two-step nucleation mechanism in solid−solid phase transitions. *Nat. Mater.* **2015**, *14*, 101−108.

(32) Wasilewski, R. J. On the nature of the martensitic transformation. *Metall. Mater. Trans. A* **1975**, *6*, 1405.

(33) Feng, C.; Guo, C.; Hu, D.; Guo, J.; Cao, X.; Akram, N.; Wang, J. Catalytic performance of Co 1,3,5-benzenetricarboxylate in the conversion of CO_2 to cyclic carbonates. *Reac. Kinet. Mech. Cat.* **2018**, *125*, 633−645.

(34) Israr, F.; Chun, D.; Kim, Y.; Kim, D. K. High yield synthesis of Ni-BTC metal−organic framework with ultrasonic irradiation: Role of polar aprotic DMF solvent. *Ultrason. Sonochem.* **2016**, *31*, 93−101.

(35) Nowacka, A.; Briantais, P.; Prestipino, C.; Llabrés i Xamena, F. X. Facile "Green" Aqueous Synthesis of Mono- and Bimetallic Trimesate Metal−Organic Frameworks. *Cryst. Growth Des.* **2019**, *19*, 4981−4989.

(36) Hu, X.; Lou, X.; Li, C.; Ning, Y.; Liao, Y.; Chen, Q.; Mananga, E. S.; Shen, M.; Hu, B. Facile synthesis of the Basolite F300-like nanoscale Fe-BTC framework and its lithium storage properties. *RSC Adv.* **2016**, *6*, 114483−114490.

(37) Yaghi, O. M.; Li, H.; Groy, T. L. Construction of Porous Solids from Hydrogen-Bonded Metal Complexes of 1,3,5-Benzenetricarboxylic Acid. *J. Am. Chem. Soc.* **1996**, *118*, 9096−9101.

(38) Li, P.-Z.; Wang, X.-J.; Li, Y.; Zhang, Q.; Tan, R. H. D.; Lim, W. Q.; Ganguly, R.; Zhao, Y. Co(II)-tricarboxylate metal−organic frameworks constructed from solvent-directed assembly for CO_2 adsorption. *Microporous Mesoporous Mater.* **2013**, *176*, 194−198.

(39) Hsu, S.-C.; Chiang, P.-H.; Chang, C.-H.; Lin, C.-H. catena-Poly[[tetraaquanickel(II)]-l3- benzene-1,3,5-tricarboxylato-30:1:2- j4 O1 :O3 ,O30 :O5 -[tetraaquanickel(II)]- l2-benzene-1,3,5-tricarboxylato2:3j2 O1 :O3 -[tetraaquanickel(II)]]. *Acta Cryst* **2009**, *65*, m625−m626.

(40) Burlak, P. V.; Samsonenko, D. G.; Kovalenko, K. A. *CSD Communication (Private Communication)* 2019, p 1952653.

(41) Horcajada, P.; Surblé, S.; Serre, C.; Hong, D.-Y.; Seo, Y.-K.; Chang, J.-S.; Grenèche, J.-M.; Margiolaki, I.; Férey, G. Synthesis and catalytic properties of MIL-100(Fe), an iron(iii) carboxylate with large pores. *Chem. Commun.* **2007**, 2820−2822.

(42) Sapnik, A. F.; Bechis, I.; Collins, S. M.; Johnstone, D. N.; Divitini, G.; Smith, A. J.; Chater, P. A.; Addicoat, M. A.; Johnson, T.; Keen, D.

A.; Jelfs, K. E.; Bennett, T. D. Mixed hierarchical local structure in a disordered metal–organic framework. *Nat. Commun.* **2021**, *12*, 2062.
(43) Kulachenkov, N. K.; Sun, D.; Mezenov, Y. A.; Yankin, A. N.; Rzhevskiy, S.; Dyachuk, V.; Nominé, A.; Medjahdi, G.; Pidko, E. A.; Milichko, V. A. Photochromic Free MOF-Based Near-Infrared Optical Switch. *Angew. Chem., Int. Ed.* **2020**, *59*, 15522–15526.
(44) Mezenov, Y. A.; Bruyere, S.; Kulachenkov, N. K.; Yankin, A. N.; Rzhevskiy, S. S.; Alekseevskiy, P. V.; Gilemkhanova, V. D.; Bachinin, S. V.; Dyachuk, V.; Krasilin, A. A.; Zollinger, J.; Belmonte, T.; Nominé, A.; Milichko, V. A. Probing the dynamics of Cu nanoparticle growth inside metal-organic frameworks upon electron beam irradiation. *Photonics Nanostructures - Fundam. Appl* **2020**, *41*, 100832.
(45) Potapov, P. L.; Kulkova, S. E.; Schryvers, D.; Verbeeck, J. Structural and chemical effects on EELS $L_{3,2}$ ionization edges in Ni–based intermetallic compounds. *Phys. Rev. B* **2001**, *64*, 184110.
(46) Zhao, Y.; Feltes, T. E.; Regalbuto, J. R.; Meyer, R. J.; Klie, R. F. In situ electron energy loss spectroscopy study of metallic Co and Co oxides. *J. Appl. Phys.* **2010**, *108*, 063704.
(47) Yao, Y.; Hu, Y.; Scott, R. W. J. Watching Iron Nanoparticles Rust: An in Situ X-ray Absorption Spectroscopic Study. *J. Phys. Chem. C* **2014**, *118*, 22317–22324.
(48) Jaji, N.-D.; Lee, H. L.; Hussin, M. H.; Akil, H. M.; Zakaria, M. R.; Othman, M. B. H. Advanced nickel nanoparticles technology: From synthesis to applications. *Nanotechnol. Rev.* **2020**, *9*, 1456–1480.
(49) Li, W.; Borkiewicz, O. J.; Saubanère, M.; Doublet, M.-L.; Flahaut, D.; Chupas, P. J.; Chapman, K. W.; Dambournet, D. Atomic Structure of 2 nm Size Metallic Cobalt Prepared by Electrochemical Conversion: An in Situ Pair Distribution Function Study. *J. Phys. Chem. C* **2018**, *122*, 23861–23866.
(50) Balela, M. D. L.; Lockman, Z.; Azizan, Z.; Matsubara, E.; Amorsolo, A. V., Jr. Protective Agent-Free Synthesis of Colloidal Cobalt Nanoparticles. *AIP Conf. Proc.* **2010**, *1217*, 113.
(51) Yang, J.; Zeng, Z.; Kang, J.; Betzler, S.; Czarnik, C.; Zhang, X.; Ophus, C.; Yu, C.; Bustillo, K.; Pan, M.; Qiu, J.; Wang, L.-W.; Zheng, H. Formation of two-dimensional transition metal oxide nanosheets with nanoparticles as intermediates. *Nat. Mater.* **2019**, *18*, 970–976.
(52) Li, D.; Nielsen, M. H.; Lee, J. R. I.; Frandsen, C.; Banfield, J. F.; De Yoreo, J. J. Direction-Specific Interactions Control Crystal Growth by Oriented Attachment. *Science* **2012**, *336*, 1014–1018.
(53) Shanbhag, P. N.; Biswas, R. K.; Pati, S. K.; Sundaresan, A.; Rao, C. N. R. Elusive Co_2O_3: A Combined Experimental and Theoretical Study. *ACS Omega* **2020**, *5*, 29009–29016.
(54) *Lawrence Berkeley National Lab, the Materials Project, Materials Data on Co_2O_3 (SG:63)*; OSTI Identifier, 2014, , 1323085.
(55) Sudhakar, P.; Radhakrishnan, T. P. Stimuli responsive and reversible crystalline–amorphous transformation in a molecular solid: fluorescence switching and enhanced phosphorescence in the amorphous state. *J. Mater. Chem. C* **2019**, *7*, 7083–7089.
(56) Ali, M. A.; Liu, X.; Sun, H.-T.; Ren, J.; Qiu, J. Metal Inorganic-Organic Complex Glass and Fiber for Photonic Applications. *Chem. Mater.* **2022**, *34*, 2476–2483.
(57) Gaillac, R.; Pullumbi, P.; Coudert, F.-X. Melting of Zeolitic Imidazolate Frameworks with Different Topologies: Insight from First-Principles Molecular Dynamics. *J. Phys. Chem. C* **2018**, *122*, 6730–6736.
(58) Gaillac, R.; Pullumbi, P.; Bennett, T. D.; Coudert, F.-X. Structure of Metal-Organic Framework Glasses by Ab Initio Molecular Dynamics. *Chem. Mater.* **2020**, *32*, 8004–8011.
(59) Kulachenkov, N. K.; Bruyere, S.; Sapchenko, S. A.; Mezenov, Y. A.; Sun, D.; Krasilin, A. A.; Nominé, A.; Ghanbaja, J.; Belmonte, T.; Fedin, V. P.; Pidko, E. A.; Milichko, V. A. Ultrafast Melting of Metal–Organic Frameworks for Advanced Nanophotonics. *Adv. Funct. Mater.* **2020**, *30*, 1908292.
(60) Chang, H.; Kim, B. H.; Jeong, H. Y.; Moon, J. H.; Park, M.; Shin, K.; Chae, S. I.; Lee, J.; Kang, T.; Choi, B. K.; Yang, J.; Bootharaju, M. S.; Song, H.; An, S. H.; Park, K. M.; Oh, J. Y.; Lee, H.; Kim, M. S.; Park, J.; Hyeon, T. Molecular-Level Understanding of Continuous Growth from IronOxo Clusters to Iron Oxide Nanoparticles. *J. Am. Chem. Soc.* **2019**, *141*, 7037–7045.
(61) Bennett, T. D.; Coudert, F.-X.; James, S. L.; Cooper, A. I. The changing state of porous materials. *Nature Mater* **2021**, *20*, 1179–1187.
(62) Pang, E. L.; Vo, N. Q.; Philippe, T.; Voorhees, P. W. Modeling interface-controlled phase transformation kinetics in thin films. *J. Appl. Phys.* **2015**, *117*, 175304.
(63) Tartaj, P.; del Puerto Morales, M.; Veintemillas-Verdaguer, S.; González-Carreño, T.; Serna, C. J. Progress in the preparation of magnetic nanoparticles for applications in biomedicine. *J. Phys. D: Appl. Phys.* **2009**, *42*, 224002.
(64) Scholten, K.; Meng, E. Electron-beam lithography for polymer bioMEMS with submicron features. *Microsyst. Nanoeng.* **2016**, *2*, 16053.
(65) Tu, M.; Xia, B.; Kravchenko, D. E.; Tietze, M. L.; Cruz, A. J.; Stassen, I.; Hauffman, T.; Teyssandier, J.; De Feyter, S.; Wang, Z.; Fischer, R. A.; Marmiroli, B.; Amenitsch, H.; Torvisco, A.; Velásquez-Hernández, J. M.; Falcaro, P.; Ameloot, R. Direct X-ray and electron-beam lithography of halogenated zeolitic imidazolate frameworks. *Nat. Mater.* **2021**, *20*, 93–99.
(66) Qin, N.; Qian, Z.-G.; Zhou, C.; Xia, X.-X.; Tao, T. H. 3D electron-beam writing at sub-15 nm resolution using spider silk as a resist. *Nature Commun* **2021**, *12*, 5133.
(67) Sheldrick, G. M. A short history of SHELX. *Acta Cryst. A* **2008**, *64*, 112–122.
(68) *XSHELL©Version 6*; Bruker AXS Inc.: Madison, Wisconsin, USA, 2004; Vol. *3.1*.
(69) Chai, J.-D.; Head-Gordon, M. Long-range corrected hybrid density functionals with damped atom–atom dispersion corrections. *Phys. Chem. Chem. Phys.* **2008**, *10*, 6615–6620.
(70) Frisch, M. J.; Trucks, G. W.; Schlegel, H. B.; Scuseria, G. E.; Robb, M. A.; Cheeseman, J. R.; Scalmani, G.; Barone, V.; Mennucci, B.; Petersson, G. A.; Nakatsuji, H.; Caricato, M.; Li, X.; Hratchian, H. P.; Izmaylov, A. F.; Bloino, J.; Zheng, G.; Sonnenberg, J. L.; Hada, M.; Ehara, M.; Toyota, K.; Fukuda, R.; Hasegawa, J.; Ishida, M.; Nakajima, T.; Honda, Y.; Kitao, O.; Nakai, H.; Vreven, T.; Montgomery, J. A., Jr; Peralta, J. E.; Ogliaro, F.; Bearpark, M.; Heyd, J. J.; Brothers, E.; Kudin, K. N.; Staroverov, V. N.; Kobayashi, R.; Normand, J.; Raghavachari, K.; Rendell, A.; Burant, J. C.; Iyengar, S. S.; Tomasi, J.; Cossi, M.; Rega, N.; Millam, N. J.; Klene, M.; Knox, J. E.; Cross, J. B.; Bakken, V.; Adamo, C.; Jaramillo, J.; Gomperts, R.; Stratmann, R. E.; Yazyev, O.; Austin, A. J.; Cammi, R.; Pomelli, C.; Ochterski, J. W.; Martin, R. L.; Morokuma, K.; Zakrzewski, V. G.; Voth, G. A.; Salvador, P.; Dannenberg, J. J.; Dapprich, S.; Daniels, A. D.; Farkas, Ö.; Foresman, J. B.; Ortiz, J. V.; Cioslowski, J.; Fox, D. J. *Gaussian 09, Revision C.01*; Wallingford CT Inc, 2009.
(71) Bader, R. F. W. A quantum theory of molecular structure and its applications. *Chem. Rev.* **1991**, *91*, 893–928.
(72) Lu, T.; Chen, F. M. A multifunctional wavefunction analyzer. *J. Comput. Chem.* **2012**, *33*, 580.